

SURFACE TEMPERATURE EFFECTS ON THE AERODYNAMIC SURFACE QUANTITIES OF HYPERSONIC CAVITY FLOW

Rodrigo C. Palharini¹; Wilson F. N. Santos¹

¹Combustion and Propulsion Laboratory (LCP), National Institute for Space Research (INPE),
Cachoeira Paulista-SP, 12630-000
rodrigo@lcp.inpe.br, wilson@lcp.inpe.br

Abstract. *Numerical simulations of two-dimensional steady hypersonic flow in a rectangular cavity at different length-to-depth (L/H) ratio and wall temperature are performed by using a Direct Simulation Monte Carlo (DSMC) method. The L/H ratio varies from 1 to 4 and wall temperature ranges from 2 to 6 times the freestream temperature. The work focuses on the effect in the aerodynamic surface quantities, such as heat transfer, pressure and skin friction coefficients due to variations in the cavity L/H ratio as well as in the wall temperature. It was found that the aerodynamic surface quantities presented a large dependence on the L/H ratio, and a small dependence on the wall temperature for the range investigated. The analysis showed that pressure and heating loads presented the maximum values along the downstream face, more precisely, at the shoulder of the cavities. Moreover, pressure and heating loads are several times larger than those for a smooth surface.*

Keywords: *Hypersonic flow, Rarefied flow, DSMC, Cavity, Aerodynamic heating*

1. INTRODUCTION

Cavity flows are of considerable importance at hypersonic speeds and feature in small-scale detail, such as surface defects, pitting and gaps in joints and between insulation tiles, and also in larger-scale features such as fuel injection slots and gaps between body surfaces and control surfaces. Usually, such defects or surface discontinuities may constitute in a potential source in a heat flux rise to the surface or even though in a premature transition from laminar to turbulent flow.

In a hypersonic vehicle design, the knowledge of the factors that affect the thermal and aerodynamic loads acting on the vehicle surface becomes imperative. Hypersonic flow over cavities may cause locally thermal and aerodynamic loads which may dramatically exceed the ones of a smooth contour, normally assumed in the thermal and aerodynamic analysis. In order to operate safely, these loads have to be predicted correctly. This can be done either by experiments, which are often very expensive for real flight conditions, or by numerical simulations, which are getting continuously increasing importance.

A lot of experiments and numerical simulations have already been conducted to investigate the flowfield structure on cavities (Bertram and Wiggs, 1963; Chapmann et al., 1958; Charwat et al., 1961a,b, 1971; Cheng and Hung, 2006; Everhart et al., 2006; Everhart, 2009; Hahn, 1969; Jackson et al., 2001; Lee and Chandra, 2006; Nestler et al., 1969; Nestler, 1982; Morgenstern Jr. and Chokani, 1994; Palharini and Santos, 2009; Plentovich et al., 1993). These research studies have been conducted in order to understand the physical aspects of a subsonic, supersonic or hypersonic flow past to this type of surface discontinuity. For the purpose of this introduction, it will be sufficient to describe only a few of these studies.

Nestler et al. (1969) conducted an experimental investigation on cavities and steps in a hypersonic turbulent flow. For the flow conditions investigated, they found that the pressure distributions in the cavity presented a typical behavior of closed cavity flow in the sense that the flow expands into the cavity, reattaches to the floor, and separates as it approaches the downstream corner.

Charwat et al. (1961a,b) performed a comprehensive study of a low supersonic cavity flow, $M_\infty \sim 3$, and postulated and verified the existence of an alternate emptying and filling of the cavity. Local heat flux to the cavity floor was also investigated. Their heat transfer measurements were made by steady-state techniques utilizing an estimated recovery temperature.

The majority of the available research studies found in the current literature has gone into considering laminar or turbulent flow over a wide range of Mach numbers in the continuum flow regime. Nevertheless, there is little understanding of the physical aspects of hypersonic flow past to cavities related to the severe aerothermodynamic environment associated to a reentry vehicle.

In this scenario, Palharini and Santos (2009) have studied cavities situated in a rarefied hypersonic flow by employing the DSMC method. The work was motivated by the interest in investigating the length-to-depth (L/H) ratio effect on the flowfield structure. The primary emphasis was to examine the sensitivity of the velocity, density, pressure and temperature due to variations on the cavity L/H ratio. The analysis showed that the recirculation region inside the cavities is a function of the L/H ratio. It was found that, for $L/H < 3$, the cavity flow structure represented that one observed in a “open” cavity. Conversely, for $L/H \geq 3$, the cavity flow structure corresponded to that of a “closed” cavity. The results showed that cavity flow behavior in the transition flow regime differs from that found in the continuum flow regime.

In continuation of the cavity study, the present account extends further the previous analysis (Palharini and Santos, 2009) by investigating the impact of the wall temperature on the aerodynamic surface quantities. In this fashion, the primary goal of this paper is to assess the

sensitivity of the heat transfer, pressure, and skin friction coefficients to variations on the wall temperature for a family of cavities defined by different L/H ratio. The focus of the present study is the low-density region in the upper atmosphere. At this condition, the degree of molecular non-equilibrium is such that the Navier-Stokes equations are inappropriate. In such a circumstance, the Direct Simulation Monte Carlo (DSMC) method will be employed to calculate the hypersonic two-dimensional flow over the cavities.

2. GEOMETRY DEFINITION

In the present account, the surface discontinuities usually present in a reentry capsule is modeled by a cavity, length L and depth H , as defined in the previous work, Palharini and Santos (2009). By considering that the depth H is much smaller than the nose radius R of a reentry capsule, i.e., $H/R \ll 1$, then the hypersonic flow over the cavity may be considered as a hypersonic flow over a flat plate with a cavity. Figure 1(a) illustrates a schematic view of the model employed.

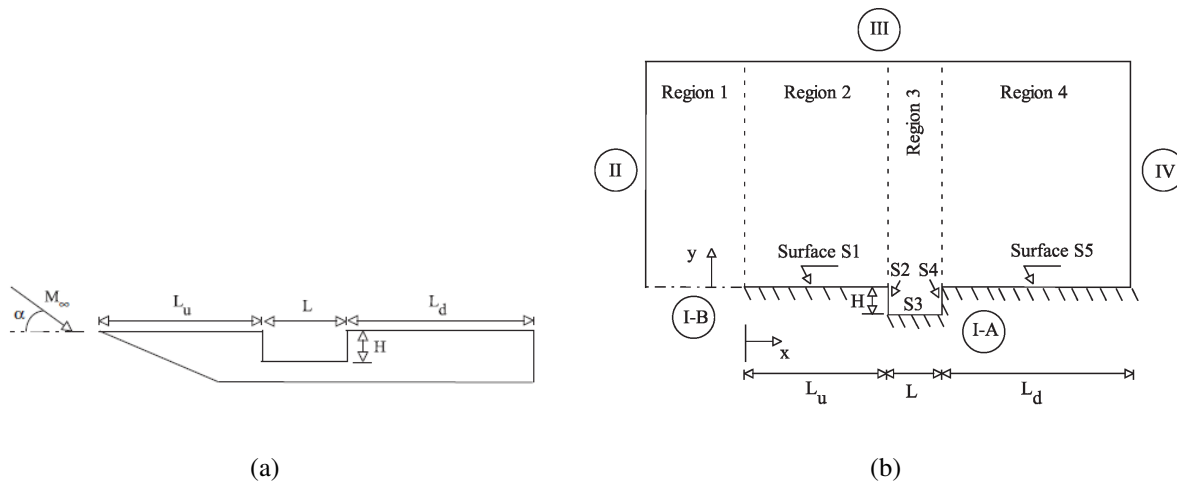


Figure 1: Drawing illustrating (a) a schematic view of the cavity configuration and (b) the computational domain.

Referring to Fig. 1(a), α stands for the angle of attack, M_∞ represents the freestream Mach number, H the cavity depth, L the cavity length, L_u the length of the cavity upstream surface, and L_d the length of the cavity downstream surface. It was assumed a depth H of 0.003 m, and a length L of 0.003, 0.006, 0.009, and 0.012 m. Therefore, the cavities investigated correspond to a length-to-depth ratio, L/H , of 1, 2, 3 and 4, respectively. In addition, L_u/λ_∞ of 50 and L_d/λ_∞ of 50, where λ_∞ is the freestream mean free path. It was considered that the flat plate is infinitely long but only the total length $L_u + L + L_d$ is investigated.

3. COMPUTATIONAL TOOL

The Direct Simulation Monte Carlo (DSMC) method, pioneered by Bird (1994), has become the standard technique for simulating low-density gas dynamics. For these flows, the computational fluid dynamics (CFD) methods that rely on continuum relations to compute the flowfield structure will not provide accurate results in the upper atmosphere, since the assumptions made in developing the differential equations, on which CFD methods are based, break down on rarefied conditions.

The DSMC method simulates real gas flows with various physical processes by means of a

huge number of modeling particles, each of which is a typical representative of a great number of real gas molecules. DSMC models the flow as being a collection of discrete particles, each one with a position, velocity and internal energy. The state of particles is stored and modified with time as the particles move, collide, and undergo boundary interactions in simulated physical space. The simulation is always calculated as unsteady flow. However, a steady flow solution is obtained as the large time state of the simulation. Therefore, the DSMC method is basically an explicit time-marching algorithm.

Collisions in the present DSMC code are modeled by using the variable hard sphere (VHS) molecular model (Bird, 1981) and the no time counter (NTC) collision sampling technique (Bird, 1989). Repartition energy among internal and translational modes is controlled by the Larsen-Borgnakke statistical model (Borgnakke and Larsen, 1975). Simulations are performed using a non-reacting gas model for a constant freestream gas composition consisting of 76.3% of N_2 and 23.7% of O_2 . Energy exchanges between the translational and internal modes, rotational and vibrational, are considered. Relaxation collision numbers of 5 and 50 were used for the calculations of rotation and vibration, respectively. For a given collision, the probabilities are designated by the inverse of the relaxation numbers, which correspond to the number of collisions necessary, on average, for a molecule to relax.

4. COMPUTATIONAL FLOW DOMAIN AND GRID

In the DSMC method, the physical space around the body is divided into an arbitrary number of regions, which are subdivided into computational cells. The cells are further subdivided into subcells, usually, two subcells/cell in each coordinate direction. The physical space network is used to facilitate the choice of molecules for collisions and for the sampling of the macroscopic flow properties such as temperature, pressure, etc. In the DSMC algorithm, the linear dimensions of the cells should be small in comparison with the scale length of the macroscopic flow gradients normal to streamwise directions, which means that the cell dimensions should be of the order of or even smaller than the local mean free path (Alexander et al, 1998, 2000). Moreover, the time step should be chosen to be sufficiently small in comparison with the local mean collision time (Garcia and Wagner, 2000; Hadjiconstantinou, 2000).

The computational domain used for the calculation is made large enough so that cavity disturbances do not reach the upstream and side boundaries, where freestream conditions are specified. A schematic view of the computational domain is illustrated in Fig. 1(b). According to this figure, side I-A is defined by the cavity surface. Diffuse reflection with complete thermal accommodation is the condition applied to this side. Side I-B is a plane of symmetry, where all flow gradients normal to the plane are zero. At the molecular level, this plane is equivalent to a specular reflecting boundary. Sides II and III are the freestream side through which simulated molecules can enter and exit. Side II is positioned at $5\lambda_\infty$ upstream of the flat-plate leading edge, and side III defined at $25\lambda_\infty$ above the flat plate. Finally, the flow at the downstream outflow boundary, side IV, is predominantly supersonic and vacuum condition is specified (Bird, 1994). As a result, at this boundary, simulated molecules can only exit.

Numerical accuracy in DSMC method depends on the grid resolution chosen as well as on the number of particles per computational cell. Both effects were investigated to determine the number of cells and the number of particles required to achieve grid independence solutions. A grid independence study was made with three different structured meshes – coarse, standard and fine – in each coordinate direction. The effect of altering the cell size in the x -direction was investigated for a coarse and fine grids with, respectively, 50% less and 100% more cells with respect to the standard grid only in the x -direction. Table 1 tabulates the number of cells employed in the four regions for coarse, standard, and fine grids for the $L/H = 1$ case.

Table 1: Number of cells in the (x -direction investigation) and [y -direction investigation] for the $L/H = 1$ case.

	Region 1	Region 2	Region 3	Region 4	Total number of cells
Coarse	(5 × 40)	(60 × 50)	(10 × 70)	(60 × 60)	7,500
	[10 × 20]	[120 × 25]	[20 × 35]	[120 × 30]	30,000
Standard	10 × 40	120 × 50	20 × 70	120 × 60	15,000
Fine	(20 × 40)	(240 × 50)	(40 × 70)	(240 × 60)	7,500
	[10 × 80]	[120 × 100]	[20 × 140]	[120 × 120]	30,000

In analogous fashion, an examination was made in the y -direction with a coarse and fine grids with, respectively, 50% less and 100% more cells with respect to the standard grid only in the y -direction. In addition, each grid was made up of non-uniform cell spacing in both directions. Moreover, point clustering is used close to solid walls and to the horizontal plane connecting the two corners. The effect (not shown) of changing the cell size in both directions on the heat transfer, pressure and skin friction coefficients was rather insensitive to the range of cell spacing considered, indicating that the standard grid, with a total of 15,000 cells, for the $L/H = 1$ case, is essentially grid independent.

A similar examination was made for the number of molecules. The standard grid for the $L/H = 1$ case corresponds to, on average, a total of 314,700 molecules. Two new cases using the same grid were investigated. These two new cases correspond to 157,500 and 630,600 molecules in the entire computational domain. As the three cases presented the same results (not shown) for the heat transfer, pressure and skin friction coefficients, hence the standard grid with a total of 314,700 molecules is considered enough for the computation of the flowfield properties.

5. FREESTREAM AND FLOW CONDITIONS

Freestream flow conditions used for the numerical simulations are those given by Palharini and Santos (2009) and summarized in Tab. 2, and the gas properties (Bird, 1994) are shown in Tab. 3. Freestream conditions represent those experienced by a capsule at an altitude of 70 km.

The freestream velocity U_∞ is assumed to be constant at 7456 m/s, which corresponds to a freestream Mach number M_∞ of 25. The translational and vibrational temperatures in the freestream are in equilibrium at 219.07 K. In order to simulate the wall temperature effect, the DSMC calculations were performed independently for three distinct numerical values of T_w , i.e., 440 K, 880 K, and 1320 K, which correspond approximately to 2, 4, and 6 times the freestream temperature T_∞ . In addition, a zero-degree angle of flow incidence was assumed in this investigation.

The overall Knudsen number Kn is defined as the ratio of the molecular mean free path

Table 2: Freestream flow conditions

Altitude (km)	T_∞ (K)	p_∞ (N/m ²)	ρ_∞ (kg/m ³)	n_∞ (m ⁻³)	λ_∞ (m)	U_∞ (m/s)
70	219.07	5.518	8.752×10^{-5}	1.8193×10^{21}	9.285×10^{-4}	7456

Table 3: Gas properties

	X	m (kg)	d (m)	ω
O_2	0.237	5.312×10^{-26}	4.01×10^{-10}	0.77
N_2	0.763	4.650×10^{-26}	4.11×10^{-10}	0.74

λ in the freestream gas to a characteristic dimension of the flowfield. In the present study, the characteristic dimension was defined as being the cavity length L . Therefore, the Knudsen number Kn_L corresponds to 0.3095, 0.1548, 0.1032, and 0.0774 for length L of 0.003, 0.006, 0.009, and 0.012 m, respectively. Finally, the Reynolds number Re_L is around 121.7, 243.4, 365.1, and 486.8 for length L of 0.003, 0.006, 0.009, and 0.012 m, respectively, also based on conditions in the undisturbed stream.

6. COMPUTATIONAL RESULTS AND DISCUSSION

This section focuses on the effects that take place in the aerodynamic surface quantities due to wall temperature variations. Aerodynamic surface quantities of particular interest in the transitional flow regime are number flux, pressure, heat transfer, and skin friction. In this fashion, the purpose of this section is to present and to discuss changes in these quantities, expressed in coefficient form, due to variations on the wall temperature as well as on the cavity L/H ratio.

In principle, as the wall temperature T_w is increased from 440 K to 1320 K, the molecules impinging on the cavity surface are reflected with greater energies. The relative translational velocities of reflected molecules close to the surface will be increased, thus reducing the net buildup of particle density near the body surface. As a result, changes in the number of molecules colliding with the surface as well as changes in the incident or reflected momentum and energy of these molecules are expected.

6.1 Number Flux

The number flux N is calculated by sampling the molecules impinging on the surface by unit time and unit area. The dependence of the number flux to variations on the L/H ratio for the $T_w = 440$ K case is illustrated in Figs. 2(a-c) for cavity surfaces $S2$, $S3$ and $S4$, respectively. In a similar way, Figs. 3(a-c) demonstrate the number flux distribution for the $T_w = 1320$ K case along the cavity surfaces $S2$, $S3$ and $S4$, respectively. In this group of plots, N_f represents the number flux N normalized by $n_\infty U_\infty$, where n_∞ is the freestream number density and U_∞ is the freestream velocity. In addition, the dimension height Y_H is the height y normalized by the cavity height H , and X' represents the distance $(x - L_u)$ normalized by the cavity length L . Also, $S2$ and $S4$ stand for the cavity vertical surfaces, i.e., upstream and downstream faces, and $S3$ for the horizontal cavity surface, i.e., the bottom surface or cavity floor, as defined in Fig. 1(b). It should be remarked that results for the $T_w = 880$ K case are intermediate to those for 440 K and 1320 K cases and, therefore, they will not be shown.

According to Figs. 2(a-c), it is seen that the dimensionless number flux N_f to the surface relies on the L/H ratio. For the upstream face, surface $S2$, the dimensionless number flux is low at the top of the cavity, and increases monotonically along the surface up to the corner at the bottom surface. Conversely, for the downstream face, surface $S4$, the dimensionless number flux depends on the L/H ratio. For the $L/H = 1$, the number flux is high at the shoulder of

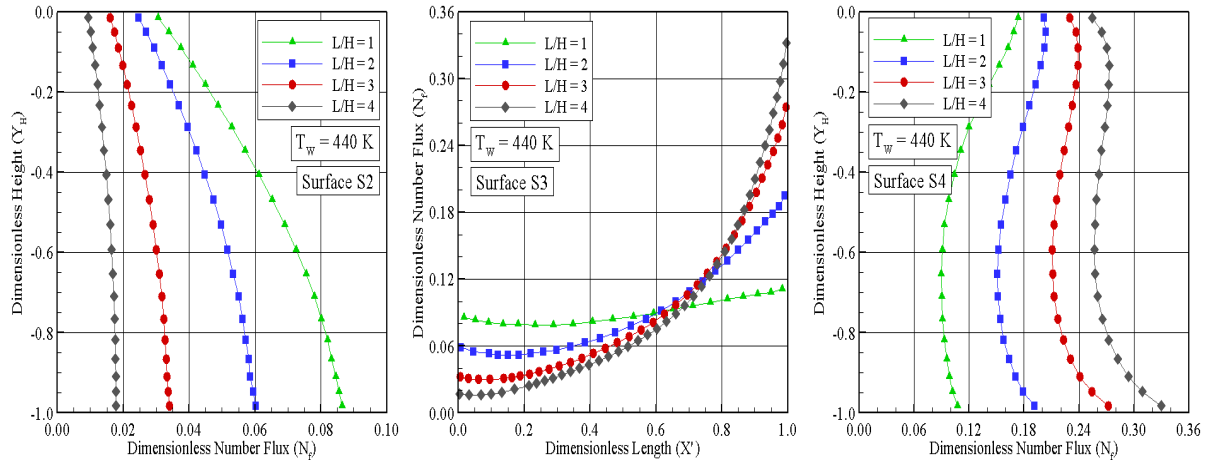


Figure 2: Dimensionless number flux (N_f) distribution along the cavity surface (a) $S2$, (b) $S3$, and (c) $S4$ for the $T_w = 440$ K case.

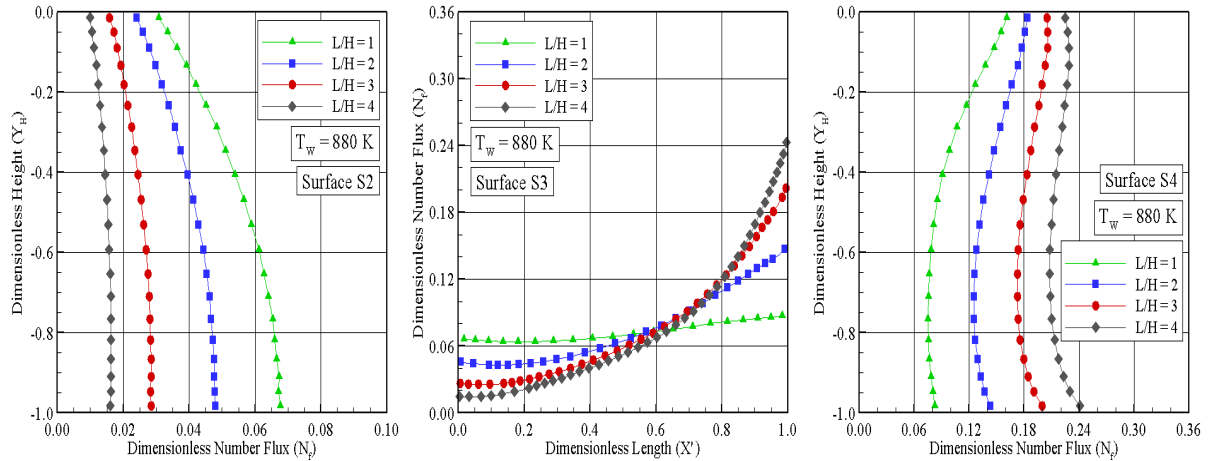


Figure 3: Dimensionless number flux (N_f) distribution along the cavity surface (a) $S2$, (b) $S3$, and (c) $S4$ for the $T_w = 1320$ K case.

the cavity, $Y_H = 0$, and decreases to a minimum value at the bottom surface. For $L/H > 1$, the number flux N_f starts increasing at the cavity shoulder, $Y_H = 0$, slightly decreases up to the station $Y_H \approx -0.6$, and increases again along the surface up to the corner at the bottom surface. Along the bottom surface, surface $S3$, the dimensionless number flux behavior also depends on L/H ratio. It basically increases along the surface with increasing the L/H ratio.

It may be recognized from Figs. 2(a-c) that in general the number flux N_f along the downstream face, surface $S4$, is one order of magnitude as compared to that along the upstream face, surface $S2$. An understanding of this behavior can be gained by considering the flow structure inside the cavity. Due to the clockwise recirculation region inside the cavities, density is low at the vicinity of the upstream face. In contrast, at the vicinity of the downstream face, the flow experiences a compression, and density is high (Palharini and Santos, 2009). Consequently, the number flux behavior is different along the two surfaces.

Referring to Figs. 3(a-c), it is observed that the number flux relies not only on the L/H ratio but also on the wall temperature. As the wall temperature is increased from 440 K to 1320 K, a reduction on the number flux to the surfaces $S2$, $S3$ and $S4$ is clearly seen. This is an expected behavior in the sense that, with increasing the body surface temperature, the molecules are reflected from the surface with greater energies. Consequently, the net buildup of particle density near the body surface is reduced.

6.2 Heat Transfer Coefficient

The heat transfer coefficient C_h is defined as follows,

$$C_h = \frac{q_w}{\frac{1}{2}\rho_\infty U_\infty^3} \quad (1)$$

where the heat flux q_w to the body surface is calculated by the net energy flux of the molecules impinging on the surface. A flux is regarded as positive if it is directed toward the body surface. The net heat flux q_w is related to the sum of the translational, rotational and vibrational energies of both incident and reflected molecules as defined by,

$$q_w = q_i + q_r = \sum_{j=1}^N \left[\frac{1}{2} m_j c_j^2 + e_{Rj} + e_{Vj} \right]_i + \sum_{j=1}^N \left[\frac{1}{2} m_j c_j^2 + e_{Rj} + e_{Vj} \right]_r \quad (2)$$

where N is the number of molecules colliding with the surface by unit time and unit area, m is the mass of the molecules, c is the velocity of the molecules, e_R and e_V stand for the rotational and vibrational energies, respectively. Subscripts i and r refer to incident and reflect molecules.

The sensitivity of the heat transfer coefficient C_h on the L/H ratio is demonstrated in Figs. 4 and 5 for wall temperature of 440 K and 1320 K, respectively. It is noticed from this set of diagrams that the heat transfer coefficient C_h is sensitive to the L/H ratio. Nevertheless, no appreciable changes are observed in the heat transfer coefficient with the wall temperature rise, for the temperature range investigated. For the upstream face, surface $S2$, the heat transfer coefficient C_h is low at the cavity shoulder, $Y_H = 0$, and increases to a maximum value close to the station $Y_H \approx -0.4$. Afterwards, it decreases along the surface up to the corner at the bottom surface. Along the cavity floor, surface $S3$, the heat transfer coefficient depends on the L/H ratio. C_h roughly increases from zero at station $X' = 0$, increases along the surface and reaches a maximum value around station $X' = 0.85$. In addition, the larger the L/H ratio is the larger the maximum value attained by the heat transfer coefficient C_h . After that, C_h drops off up to the $S3/S4$ surface junction. For the downstream face, surface $S4$, the heat transfer coefficient is high at the top of the cavity, and monotonically decreases along the surface, reaching very lower values at the corner. It is also very encouraging to observe that the heat transfer coefficient C_h for the downstream face is roughly one order of magnitude larger than that for the bottom surface, and this is one order of magnitude larger than that for the upstream face. One possible reason for that is because at the vicinity of the upstream face the flow experiences a expansion. In contrast, at the vicinity of the downstream face, it experiences a compression due to the recirculation structure inside the cavity (Palharini and Santos, 2009).

The heat flux to the body surface was defined in terms of the incident and reflected flow properties, Eq.(2), and based upon the gas-surface interaction model of fully accommodated, complete diffuse re-emission. The diffuse model assumes that the molecules are reflected equally in all directions, quite independently of their incident speed and direction. Due to the

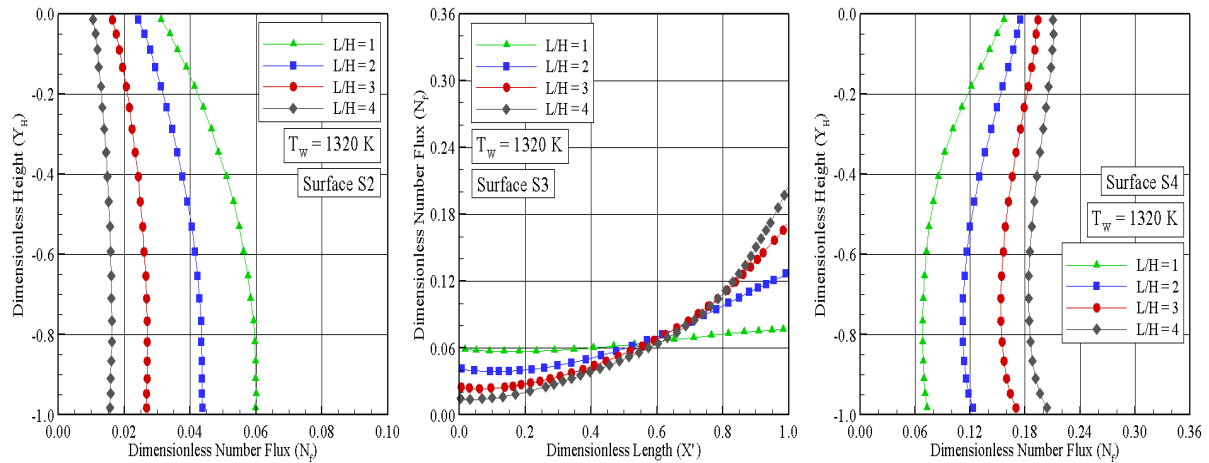


Figure 4: Heat transfer coefficient (C_h) distribution along the cavity surface (a) S_2 , (b) S_3 , and (c) S_4 for the $T_w = 440$ K case.

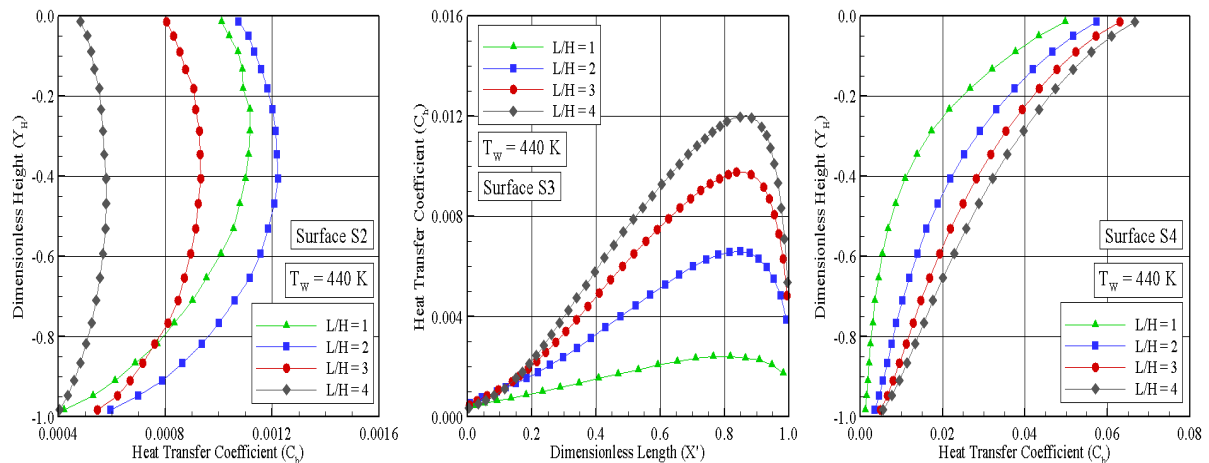


Figure 5: Heat transfer coefficient (C_h) distribution along the cavity surface (a) S_2 , (b) S_3 , and (c) S_4 for the $T_w = 1320$ K case.

diffuse reflection model, the reflected velocity of the molecules impinging on the body surface is obtained from a Maxwellian distribution that takes into account for the temperature of the body surface. In this fashion, according to Eq.(2), not only the number of molecules impinging on the surface but also the wall temperature plays a important role on the reflected contribution to the net heat flux to the body surface.

Of particular interest is the behavior of the heat transfer coefficient C_h along the lower half part of upstream and downstream faces, surfaces S_2 and S_4 , Figs. 4(a,c) and 5(a,c). It is clearly noticed that C_h decreases up to the bottom surface, i.e., from $Y' = -0.4$ to $Y' = -1.0$. As the number of molecules impinging on the lower half part of these cavity surfaces decreases, as shown by Figs. 2(a,c) and 3(a,c), then the velocity of the molecules increases in this region in order to increase the heat transfer coefficient in this region.

At this point it is worth taking a closer look at these results. In order to do that, the peak

values for the heat transfer coefficient C_h , approximately 0.050 and 0.062 for the L/H ratio of 1 and 4, respectively, at the cavity shoulder, are compared to that predicted for a smooth surface, i.e., a flat plate without a cavity. According to Leite and Santos (2009), for the same freestream conditions and wall temperature of 880 K, the maximum value for C_h is around to 0.029 at a station $8.4\lambda_\infty$ from the leading edge. Therefore, the peak value of C_h for the cavity is around twice of that for a smooth surface.

6.3 Pressure Coefficient

The pressure coefficient C_p is defined as follows,

$$C_p = \frac{p_w - p_\infty}{\frac{1}{2}\rho_\infty U_\infty^2} \quad (3)$$

where the pressure p_w on the body surface is calculated by the sum of the normal momentum fluxes of both incident and reflected molecules at each time step as follows,

$$p_w = p_i + p_r = \sum_{j=1}^N \{[(mv)_j]_i + [(mv)_j]_r\} \quad (4)$$

where v is the velocity component of the molecule j in the surface normal direction.

The effect on pressure coefficient C_p due to variations on the L/H ratio is demonstrated in Figs. 6 and 7 for wall temperature of 440 K and 1320 K, respectively.

Looking first to Figs. 6(a-c), it is seen that the pressure coefficient C_p roughly follows the same trend as that presented by the number flux in the sense that, for the upstream face, surface $S2$, it is low at the shoulder, $Y' = 0$, and increases downward along the surface, reaching the maximum value at the bottom, station $Y' = -1.0$. In the following, for the cavity floor, surface $S3$, the pressure coefficient increases along the entire surface, and reaches the maximum value at the vicinity of the $S3/S4$ surface junction. Finally, along the downstream face, surface $S4$, the pressure coefficient behavior is in contrast to that observed along the surface $S2$ in the sense that C_p presents the lower value at the station $Y' = -1.0$, and increases monotonically upward along the surface, reaching the peak value at the shoulder, $Y' = 0$. It may be inferred in passing that this is an expected behavior since the flow within the cavity is characterized by the appearance of a recirculation region. According to Palharini and Santos (2009), the streamline pattern shows that the flow is characterized by a primary vortex system for the $L/H = 1$ and 2 cases, where a clockwise recirculating structure fills the entire cavities. Conversely, for the $L/H = 3$ and 4 cases, the flow is characterized by two vortex systems at the vicinity of the upstream and downstream surfaces, with the freestream flow reaching the cavity floor, surface $S3$.

Turning next to Figs. 7(a-c), it is found that the wall temperature rise has no expressive effect on the pressure coefficient C_p for the temperature range investigated. It is seen that the pressure coefficient slightly increases along the surfaces $S2$, $S3$ and $S4$. It may be concluded from Eq. (3) that a pressure coefficient rise is associated to an increase in the wall pressure p_w . In addition, based on Eq. (4), a wall pressure rise is related to an increase in the number of molecules colliding to the surface and/or an increase in the velocity of the molecules. At this point, it is important to recognize from the number flux distribution, Figs. 2 and 3, that the number flux to the surfaces decreased with increasing the wall temperature. In addition, with increasing the wall temperature, the molecules are reflected with more energy. Therefore,

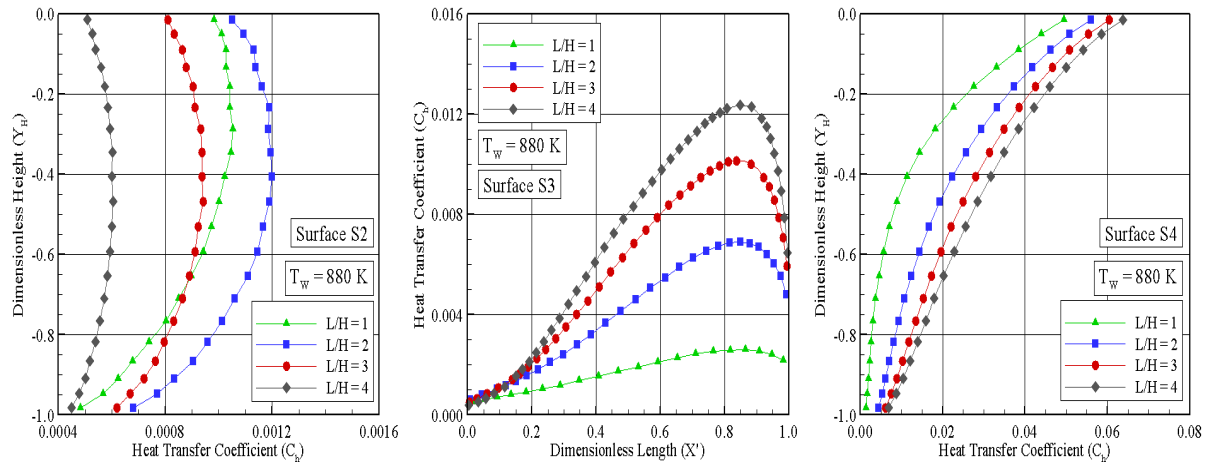


Figure 6: Pressure coefficient (C_p) distribution along the cavity surface (a) S_2 , (b) S_3 , and (c) S_4 for the $T_w = 440$ K case.

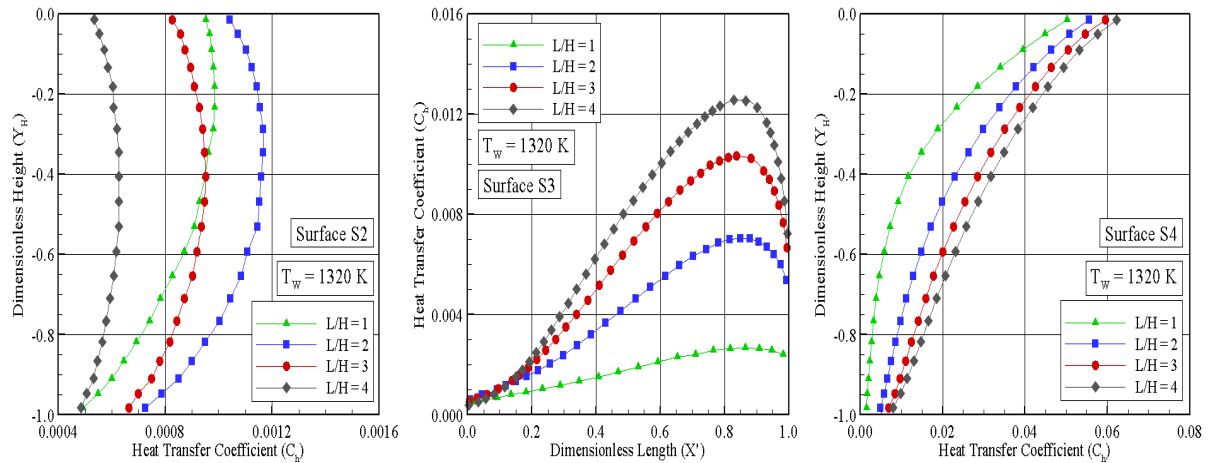


Figure 7: Pressure coefficient (C_p) distribution along the cavity surface (a) S_2 , (b) S_3 , and (c) S_4 for the $T_w = 1320$ K case.

there is an indication that the energetic scattered molecules play a more significant role, with the incident component of the wall pressure decreasing and the reflected one increasing with the wall temperature rise. Hence, the insensitivity of the pressure coefficient to wall temperature variations for the range investigated, shown in Figs. 7(a-c), is primarily attributed to a counterbalance between the number flux reduction and the normal momentum rise related to the reflected molecules.

In the following, it proves helpful to compare the maximum values for the pressure coefficient observed in the cavities with that of a smooth surface, i.e., a flat plate without a cavity. As a basis of comparison, for the $L/H = 4$ case, the pick values for C_p is around 0.1 and 0.2 observed at the cavity floor, surface S_3 , and at the cavity shoulder, surface S_4 . According to Leite and Santos (2009), for the same freestream conditions and wall temperature of 880 K, the maximum value for C_p is around to 0.039 at a station $24.2\lambda_\infty$ from the leading edge. Therefore, the

peak value of C_p for the cavity is around one order of magnitude larger than that for a smooth surface.

6.4 Skin Friction Coefficient

The skin friction coefficient C_f is defined as follows,

$$C_f = \frac{\tau_w}{\frac{1}{2}\rho_\infty U_\infty^2} \quad (5)$$

where the shear stress τ_w on the body surface is calculated by the sum of the tangential momentum fluxes of both incident and reflected molecules impinging on the surface at each time step by the following expression,

$$\tau_w = \tau_i + \tau_r = \sum_{j=1}^N \{[(mu)_j]_i + [(mu)_j]_r\} \quad (6)$$

where u is the velocity component of the molecule j in the surface tangential direction.

It is worthwhile to note that for the special case of diffuse reflection, the gas-surface interaction model adopted herein, the reflected molecules have a tangential moment equal to zero, since the molecules essentially lose, on average, their tangential velocity components. In this fashion, the net tangential momentum flux is defined as follows,

$$\tau_w = \tau_i = \sum_{j=1}^N \{[(mu)_j]_i\} \quad (7)$$

The impact of the L/H ratio on the skin friction coefficient C_f is depicted in Figs. 8 and 9 for wall temperature of 440 K and 1320 K, respectively. According to this set of plots, it is noticed that, for the upstream face, surface $S2$, the skin friction coefficient in general presents the peak value at the shoulder, $Y' = 0$, decreases downward along the surface up to station $Y' \approx -0.75$, and basically reaches a negative constant value along the remaining part of the surface. In what follows, for the cavity floor, surface $S3$, the skin friction coefficient behavior relies on the L/H ratio. It is negative near the vicinity of the $S2/S3$ surface junction, then it becomes positive and reaches a maximum value as a function of the L/H ratio. Finally, along the downstream face, surface $S4$, the skin friction coefficient increases negatively upward along the entire surface. Usually, as C_f changes from positive to negative value, the condition $C_f = 0$ may indicate the presence of a backflow, an attachment or reattachment point in the flow. In the present account, these changes are directly related to the clockwise recirculation structure, defined by a primary vortex system observed for the $L/H = 1$ and 2 cases, and two recirculating structures observed for the $L/H = 3$ and 4 cases, where the flow is characterized by two vortex systems at the vicinity of the upstream and downstream faces. As a result, the skin friction coefficient distribution along the bottom surface, $S3$, is similar for the $L/H = 1$ and 2 cases. In addition, the distribution for the $L/H = 3$ case presents the same behavior for the $L/H = 4$ case.

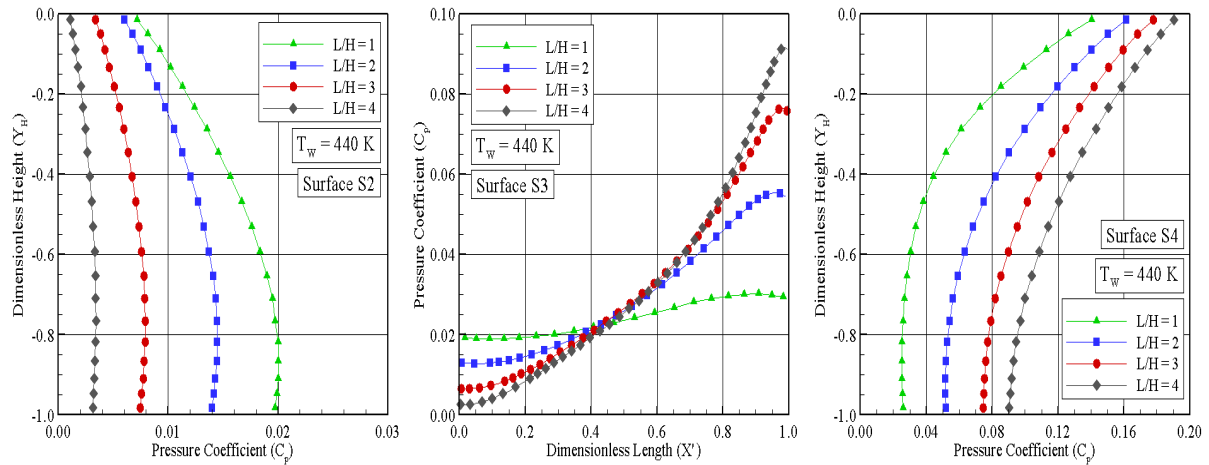


Figure 8: Skin friction coefficient (C_f) distribution along the cavity surface (a) S_2 , (b) S_3 , and (c) S_4 for the $T_w = 440$ K case.

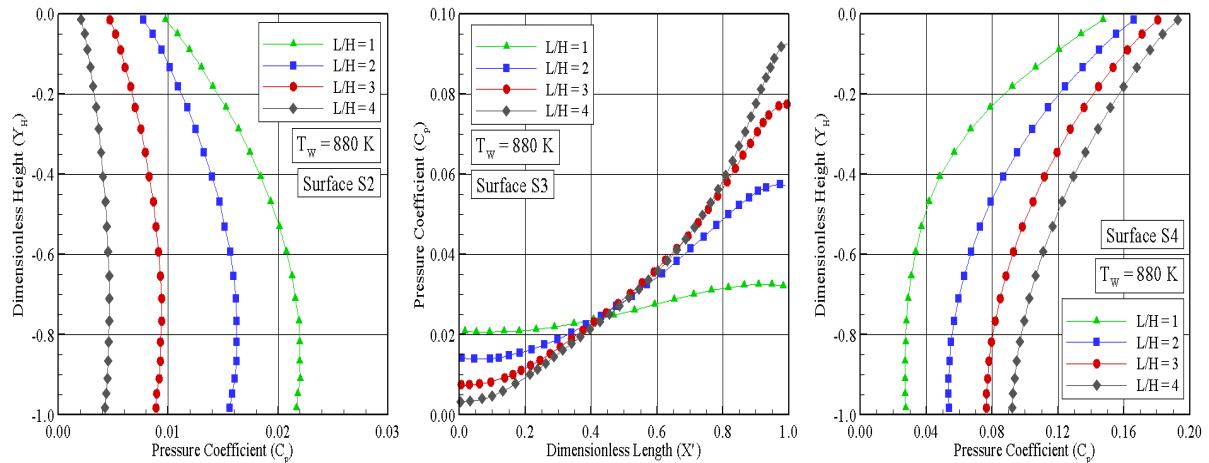


Figure 9: Skin friction coefficient (C_f) distribution along the cavity surface (a) S_2 , (b) S_3 , and (c) S_4 for the $T_w = 1320$ K case.

7. CONCLUDING REMARKS

Computations of a rarefied hypersonic flow on a family of cavities have been performed by using the Direct Simulation Monte Carlo (DSMC) method. The calculations provided information concerning the nature of the aerodynamic surface quantities action on the cavity surfaces. Effects of the length-to-depth ratio and effects of the wall temperature on the number flux, heat transfer, pressure and skin friction coefficients for a representative range of parameters were investigated. The wall temperature varied from 440 K to 1320 K, and the length-to-depth ratio ranged from 1 to 4, which corresponded Knudsen numbers in the transitional flow regime.

On the basis of the foregoing results it can be concluded that, for the range of the conditions investigated in the present study, the aerodynamic quantities acting on the cavity surface depend on the L/H ratio. In contrast, the aerodynamic surface quantities presented a small dependence on the wall temperature. It was found that the pressure load and the heat load presented the

maximum values along the downstream face of the cavities, more precisely, at the shoulder of the cavities. In addition, these loads are much larger than those attained in a smooth surface.

ACKNOWLEDGEMENTS

The authors would like to thank the financial support provided by FAPESP (Fundação de Amparo a Pesquisa do Estado de São Paulo) under Grant No. 2007/57673-6.

Bibliografia

- Alexander, F. J., Garcia, A. L., and Alder, B. J., 1998. Cell Size Dependence of Transport Coefficient in Stochastic Particle Algorithms. *Physics of Fluids*, 10, pp. 1540–1542.
- Alexander, F. J., Garcia, A. L., and Alder, B. J., 2000. Erratum: Cell Size Dependence of Transport Coefficient in Stochastic Particle Algorithms. *Physics of Fluids*, 12, pp. 731–731.
- Bertram, M. H., and Wiggs, M. M., 1963. Effect of Surface Distortions on the Heat Transfer to a Wing at Hypersonic Speeds. *AIAA Journal*, 1, pp. 1313–1319.
- Bird, G. A., 1981. Monte Carlo Simulation in an Engineering Context. In Fisher, S. S., ed., *Progress in Astronautics and Aeronautics: Rarefied gas Dynamics*, Vol. 74, part I, AIAA New York, pp. 239–255.
- Bird, G. A., 1989. Perception of Numerical Method in Rarefied Gasdynamics. In Muntz, E. P., Weaver, D. P., and Capbell, D. H., eds., *Rarefied Gas Dynamics: Theoretical and Computational Techniques*, Vol. 118, Progress in Astronautics and Aeronautics, AIAA, New York, pp. 374–395.
- Bird, G. A., 1994. *Molecular Gas Dynamics and the Direct Simulation of Gas Flows*, Oxford University Press.
- Borgnakke, C. and Larsen, P. S., 1975. Statistical Collision Model for Monte Carlo Simulation of Polyatomic Gas Mixture. *Journal of Computational Physics*, 18, pp. 405–420.
- Chapmann, D. R., Kuehn, D. M., and Larson, H. K., 1958. Investigation of Separated Flows in Supersonic and Subsonic Streams with Emphasis on the Effect of Transition. *NACA Report 1356*.
- Charwat, A. F., Dewey, C. F., Roos, and J. N., Hitz, J. A., 1961. An Investigation of Separated Flows – Part I: The Pressure Field. *Journal of Aerospace Sciences*, 28, pp. 457–470.
- Charwat, A. F., Dewey, C. F., Roos, and J. N., Hitz, J. A., 1961. An Investigation of Separated Flows – Part II: Flow in the Cavity and Heat Transfer. *Journal of Aerospace Sciences*, 28, pp. 513–527.
- Charwat, A. F., 1971. Separation of a Supersonic Accelerated Flow over Notches. *AIAA Journal*, 9, pp. 1656–1657.
- Cheng, M. and Hung, K. C., 2006. Vortex Structure of Steady Flow in a Rectangular Cavity. *Computers and Fluids*, 35, pp. 1046–1062.
- Everhart, J. L., Alter, S. J., Merski, N. R., and Wood, W. A., 2006. Pressure Gradient Effects on Hypersonic Cavity Flow Heating. *44th AIAA Aerospace Sciences Meeting and Exhibit*, AIAA Paper 2006–0185, Reno, NV.
- Everhart, J. L., 2009. Supersonic/Hypersonic Laminar heating Correlations for Rectangular and Impact-Induced Open and Closed Cavities. *Journal of spacecraft and Rockets*, 46, pp. 545–560.
- Garcia, A. L., and Wagner, W., 2000. Time Step Truncation Error in Direct Simulation Monte Carlo. *Physics of Fluids*, 12, pp. 2621–2633.
- Hadjiconstantinou, N. G., 2000. Analysis of Discretization in the Direct Simulation Monte Carlo. *Physics of Fluids*, 12, pp. 2634–2638.

- Hahn, M., 1969. Experimental Investigation of Separated Flow over a Cavity at Hypersonic Speed. *AIAA Journal*, 7, pp. 1092–1098.
- A. P. Jackson, A. P., Hillier, R., and Soltani, S., 2001. Experimental and Computational Study of Laminar Cavity Flows at Hypersonic Speeds. *Journal of Fluid Mechanics*, 427, pp. 329–358.
- Lee, G., and Chandra, S., 2006. Numerical Analysis of Heat Transfer Enhancement from Surfaces with Cavities. *44th AIAA Aerospace Sciences Meeting and Exhibit*, AIAA Paper 2006–0186.
- Leite, P. H. M., and Santos, W. F. N., 2009. Direct Simulation of Heat Transfer and Pressure Distributions of Hypersonic Flow over a Backward-Facing Steps. *XII Encontro de Modelagem Computacional*, EMC 2009, December 2–4, Rio de Janeiro, RJ.
- Nestler, D. E., Saydah, A. R., and Auxer, W. L., 1969. Heat Transfer to Steps and Cavities in Hypersonic Turbulent Flow. *AIAA Journal*, 7, pp. 1368–1370.
- Nestler, D. E., 1982. An Experimental Study of Hypersonic Cavity Flow. *Journal of Spacecraft and Rockets*, 19, pp. 195–196.
- Morgenstern Jr., A., and N. Chokani, N., 1994. Hypersonic Flow Past Open Cavities. *AIAA Journal*, 32, pp. 2387–2393.
- Palharini, R. C., and Santos, W. F. N., 2010. Computational Analysis of Hypersonic Flow over Cavities. *3rd Southern Conference on Computational Modeling*, Rio Grande, RS, Nov. 23–25 Nov.
- Plentovich, E. B., Stallings, R. L., and Tracy, M. B., 1993. Experimental Cavity Pressure Measurements at Subsonic and Transonic Speeds. *NASA Technical Report*, No. TP-3358.

PERMISSION

The authors are the only responsible for the printed material included in this paper.